MULTI-OBJECTIVE OPTIMIZATION OF A SOLAR PARTICLE RECEIVER COUPLED TO A THERMAL ENERGY STORAGE SYSTEM

J.A. Moctezuma Hernández[a], R.P. Merchán[a], J. García-Ferrero[a], J.M.M. Roco[a]

[a] *Applied Physics Department and IUFFyM, Universidad de Salamanca, Plaza de la Merced S/N, Spain, Phone: +34 923 294*

Abstract:

Solar particle receivers combined with thermal energy storage are a promising route to improve dispatchability in high-temperature concentrated solar power. This work investigates an integrated configuration in which a fluidized-bed solar particle receiver charges a packed-bed thermal energy storage unit through an intermediate heat exchanger, while discharge is coupled to an sCO_2 Brayton cycle with ORC bottoming recovery. A dynamic thermodynamic model is developed using real solar irradiance data from Seville, and the system is assessed through multi-objective optimization by maximizing round-trip efficiency and stored energy density. The results show that solar charging generates a marked axial thermal stratification in the packed bed, enabling high storage capacity but also conditioning the discharge process. During discharge, the Brayton cycle provides the main power output, whereas the ORC recovers residual heat and contributes to a smoother overall response. The Pareto front reveals the expected trade-off between storage density and energy recovery, and TOPSIS is used to identify a compromise solution. Overall, the study highlights the potential of solar particle receiver–packed-bed TES systems for dispatchable CSP while identifying heat exchanger losses, storage thermal losses, and conversion irreversibilities as the main performance limitations.

Keywords: Solar particle receiver; Packed-bed; Concentrated solar power; Multi-objective optimization; Round-trip.

1. Introduction

The global energy transition is advancing rapidly, with renewables accounting for 92.5% of total power capacity expansion worldwide in 2024; however, energy-related CO_2 emissions still reached a record 37.8 Gt in the same year. This contrast highlights that decarbonization requires not only the deployment of renewable generation, but also efficient and dispatchable energy systems. In this context, concentrated solar power (CSP) becomes especially attractive because, unlike other variable renewable technologies, it can be directly coupled with thermal energy storage (TES), enabling the decoupling of solar energy collection from electricity production, improving dispatchability, and extending plant operating hours.

Recent research has addressed several key elements of high temperature CSP-TES-power-block integration. Trevisan *et al*. [1] proposed an indirect air driven CSP plant coupled to a packed bed TES and a supercritical CO_2 (sCO_2) Brayton cycle, evaluating its thermo-economic performance through multi-objective optimization. Cu *et al*. [2] developed a CSP system integrating a particle-sCO_2 fluidized-bed heat exchanger with a recompression sCO_2 Brayton cycle, combining sensitivity analysis with thermodynamic and economic assessment. Liang *et al*. [3] investigated the simultaneous optimization of a CSP-integrated sCO_2 Brayton–ORC system, showing the benefit of recovering low-grade waste heat through a bottoming cycle. Battisti et al. [4] analyzed the transient thermal-hydraulic performance of packed-bed TES systems operating with sCO_2, identifying the strong influence of design and operating parameters on charge–discharge efficiency. At a broader level, Pascual *et al*. [5] reviewed TES–CSP integration routes and emphasized the strategic importance of advanced storage materials and higher-temperature power blocks for next-generation plants. More recently, Qiu *et al*. [6] performed a triple-objective optimization of regenerative and recompression SCO_2 Brayton cycles for next-generation solar towers above 700 °C, highlighting the trade-off between thermal efficiency, specific work, and heat-storage temperature difference.

Despite these advances, limited attention has been given to integrated configurations combining a solar particle receiver, an intermediate heat exchanger, a packed-bed TES with different working and storage media, and a discharge stage based on an sCO_2 Brayton cycle coupled to an ORC. In the present work, a fluidized-bed solar receiver using silicon carbide particles is coupled to a packed-bed TES charged through argon and magnetite rocks, while the discharge process is connected to an sCO_2 Brayton cycle and an ORC bottoming cycle. Therefore, this study focuses on the multi-objective optimization of this hybrid configuration in order to improve solar to thermal charging, storage utilization, and power recovery during discharge.

2. 2 SYSTEM DESCRIPTION.

In Figure 1a, the schematic of the fluidized bed solar receiver is shown. This bed is composed of air and silicon carbide (SiC) particles. The receiver is coupled to a packed bed thermal energy storage system. A heat exchanger is required because the working fluid entering the packed bed is argon, whereas the thermal storage material consists of magnetite rocks. Real solar irradiance data from the city of Seville are used. The charging process is carried out over 4 hours, during which the solar resource remains stable. In this work, the best day of the year is considered, corresponding to day 216. The behavior of the solar irradiance is presented in the following section. Figure 1b shows the packed bed during the discharge process. In this case, it is coupled to a supercritical CO_2 Brayton cycle and an ORC cycle. The discharge process is performed by compressing the CO2 to a region in which the fluid reaches supercritical conditions. This takes place in the compressor and, at its outlet (state 2), the CO_2 enters two heat recuperators: a low-temperature recuperator (LTR) and a high-temperature recuperator (HTR). It then enters the packed bed, where it takes advantage of the high temperature of the system resulting from the charging process provided by the solar receiver, corresponding to state x. At the outlet of the packed bed, the fluid enters the gas turbine at high temperature, where work is produced due to fluid expansion. Since the fluid still retains thermal potential at the turbine outlet, it releases energy in the HTR and LTR heat exchangers before entering the ORC heat exchanger (HEX-2). There, heat is transferred to the ORC working fluid in order to take advantage of this residual energy. Table 1 shows the thermodynamic properties of the different materials used in each subsystem.

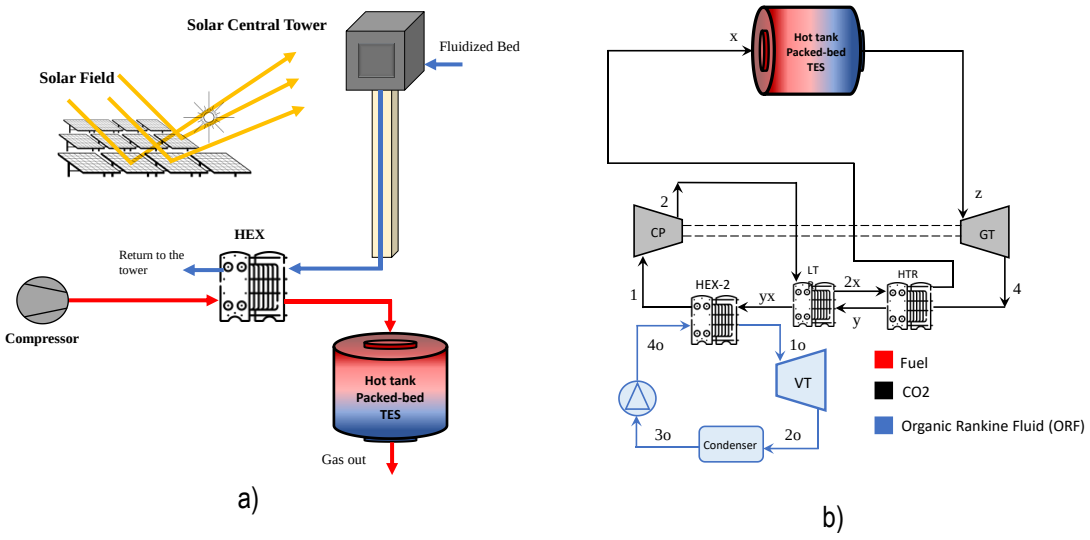

Figure 1: a) Schematic of the packed bed loading process connected to a central solar tower. b) Discharging of the packed bed using a supercritical CO_2 Brayton cycle.

Table 1: Input data for storage cycle and packed bed analysis.

Subsystem	Parameters	Value
Solar receiver (SiC)	Sauter mean diameter (d_p)	63.9 µm
	Density (ρ_p)	3210 $kg\ m^{-3}$
	Thermal conductivity (at 500°C)	109 $Wm^{-1}K^{-1}$
	Minimum fluidization velocity (u_{mf})	5.5 mm/s
Packed bed	Column height	1.2 m
	Tube diameter	11.6 m
	Inlet pressure	3.5 bar (Charging); 3.0 bar (Discharging)
	Mass flow ($\dot{m}_{PB}$)	43.63 kg/s
Magnetite (Fe_3O_4)	d_p	20 mm
	ρ_s	5173 kg/m^3

	$c_{p,s}$	$608.91 + 1.424T - 0.0015T^2 - 3.88e^{-6}T^3 + 1.036e^{-8}T^4$
	k_s	$6.22 - 0.0048T - 6.04e^{2}T^2 + 9.602e^{-9}T^3$

3. MODELING

3.1 Solar system

Both the heliostat field and the solar receiver models considered in the present work have been widely described in previous works [7] and [8] respectively, by this work authors. The heliostat field efficiency was computed based on the methodology developed in [5] for a surrounding heliostat field of 873, 120 m^2-heliostats disposed around a 150 m height tower. The solar radiation data used in this study correspond to measurements taken throughout the day in the city of Seville (Spain) [9]. Consequently, the thermal power of the heliostat field (Q thermal) varies, causing the temperature of the fluidized bed at the receiver outlet to change as well. The solar receiver was modeled as a bundle of vertical tubes traversed by a dense particle suspension (DPS) of silicon carbide (SiC) particles, fluidized with air. The other parameters used in the solar receiver are listed in Table 1.

3.2 Compressor.

The characterization of the compressor is based on isentropic efficiency, η_{is}. According to ref [10], an isentropic efficiency of 97.5% is proposed, which is adopted in this study. A reciprocating compressor is modeled due to its ability to handle high pressures, process specialized gases, and maintain high efficiency within low-capacity operating ranges. In this work, the isentropic efficiency is assumed to be the same for all turbomachinery components, both during the charging and discharge phases. On the other hand, real gases deviate from the behavior predicted by ideal gas laws, particularly when approaching the saturation curve. In such cases, a more accurate and direct approach involves considering that the compression work in an adiabatic process corresponds to the enthalpy difference. For a reversible adiabatic process, this specifically aligns with the isentropic enthalpy difference, which is calculated using Eq. (1). The compression work will be higher than ideal due to the number of different losses compared to an isentropic case. Therefore, the compressor shaft power can be expressed as calculated in Eq. (2).

$$W_{is} = h_{2s} - h_1 \tag{1}$$

$$Pot_{comp} = \frac{\dot{m}_{PB} W_{is}}{\eta_{is}} \tag{2}$$

3.3 Heat Exchanger.

The heat exchanger performance is based on the efficiency evaluation, ϵ_{HX} [10-11]. In this work, a value of $\epsilon_{HX} = 0.70$ is used [12]. In Eq. (4), the energy balance between the fluidized bed and the working fluid of the packed bed is shown.

$$\dot{m}_{DPS} C_{p,DPS} (T_{Hot\ Paticles} - T_{Cold\ Particles}) = \epsilon_{HX} \dot{m}_{PB} (h_3 - h_2) \tag{3}$$

Where $\dot{m}_{DPS}$ is the mass flow rate of the fluidized bed of the particle receiver. $T_{Hot\ Paticles}$, is the temperature at the outlet of the particle receiver. $T_{Hot\ Paticles}$ is the temperature at the outlet of the heat exchanger. The fluidized bed side which is a mixture of Silicon Carbide with air is described in Ref [7].

3.4 Hot tank (Packed bed) and Cold tank.

The governing equations describing the energy transfer process in the form of heat within the packed bed are Eq. (4) and (5). Equation (4) serves to model the fluid temperature behavior and Eq. (5) serves to model the

solid phase of the system. These equations were discretized using the centered finite difference technique and solved using the Runge-Kutta implicit method.

$$\varepsilon\rho_f c_{p,f}\frac{\partial T_f}{\partial t}+\varepsilon\rho_f\rho c_{p,f}u_f\frac{\partial T_f}{\partial x}=h_v(T_s-T_f)-\frac{A_c}{V_{tank}}U_w(T_f-T_\infty) \quad (4)$$

$$(1-\varepsilon)\rho_s c_{p,s}\frac{\partial T_s}{\partial t}=k_s\frac{\partial^2 T_s}{\partial x^2}+h_v(T_s-T_f) \quad (5)$$

Where $c_{p,f}$ and $c_{p,s}$ are the specific heat of the fluid and gas, respectively. u_f is the fluid velocity. A_c is the surface area of the storage tank. V_{tank} is the volume of the storage tank. U_w is the overall heat transfer coefficient of the storage tank wall. The volume fraction is denoted by ε, which can be evaluated as a function of the ratio of the particle diameter, d_p, and the packed bed diameter, D [13].

$$\varepsilon=0.375+0.17\,\frac{d_p}{D}+0.39\left(\frac{d_p}{D}\right)^2 \quad (6)$$

The parameter h_v is the volumetric heat transfer coefficient, the Coutier and Farber correlation [14] is used to calculate it, this can be seen in the Eq. (7).

$$h_v=700\left(\frac{G}{d_p}\right)^{0.76} \quad (7)$$

Next, the pressure drop inside the packed bed is analyzed by the Ergun and Orning (1949) equation, as shown in Eq. (8).

$$\frac{\Delta P}{L}=\frac{150\mu}{\psi^2 d_p^2}\frac{(1-\varepsilon)^2}{\varepsilon^3}\,u_f+\frac{1.75\,\rho_f}{\psi d_p}\frac{(1-\varepsilon)}{\varepsilon^3}u_f^2 \quad (8)$$

Where L is the length of the packed bed, μ is the dynamic viscosity of the fluid and ψ is the shape factor to correct for the fact that the material is not fully spherical. Finally, the analysis of the cold tank is performed by Eq. (9), where an energy balance is performed on the device.

$$\dot{Q}_{cold}=\dot{m}_{PB}(h_5-h_1) \quad (9)$$

3.5 Power Block

By performing mass and energy balances on each component of the CO2 Brayton cycle and the Organic Rankine Cycle, that is, by applying Eqs. (10) and (11), the thermodynamic analysis of the cycle is is conducted.

$$\sum\dot{m}_{in}=\sum\dot{m}_{out} \quad (10)$$

$$\sum\dot{Q}+\sum\dot{m}_{in}h_{in}=\sum\dot{W}+\sum\dot{m}_{out}h_{out} \quad (11)$$

3.6 Thermodynamic performance indicator.

The roundtrip efficiency (RTE) is in charge of analyzing the energy performance of the thermal energy storage system, which is defined as the ratio of net work at discharge to net work at charging, which is calculated as follows [13] and the stored energy density, which is calculated as shown in Eq. (12).

$$RTE=\frac{E_{discharging}}{E_{charging}}=\frac{(Pot_{comp,dis}-\dot{W}_{exp,dis})t_{dis}}{(\dot{W}_{exp,char}-Pot_{comp,char})t_{char}} \quad (12)$$

$$\rho_e=\frac{E_{discharging}}{V_{PB}} \quad (13)$$

3.7 Multi-objective optimization

The multi-objective optimization was performed using NSGA-II, a widely used method for approximating the Pareto front and handling constrained nonlinear problems. The problem is defined as:

$$max\ (f_1(x), f_2(x)) \tag{14}$$

$$subject\ to\ x\ \in\ X \tag{15}$$

where x is the decision vector and X is the feasible set. The seven decision variables were the packed bed diameter D, packed bed length L, particle diameter dp, fluid velocity uf, in the charging process, the Brayton-cycle pressure ratio rp, and the pressure-level variable P10 and P11. The objective functions were to maximize RTE and storage density. NSGA-II was implemented following Deb et al. [14], who improved the original NSGA [15] by reducing computational cost and introducing the crowded-comparison operator to rank nondominated solutions. The adopted parameters were a population size of 50, an SBX crossover probability of 95%, a polynomial mutation probability of 1/(number of variables), and a stopping criterion of 500 generations.

4. VALIDATION OF THE MODEL

The validation of the particle receiver was performed based on the work of Reyes-Belmonte *et al*. [16], where different parameters such as convective coefficient, particle mass flow, number of tubes and heat absorption area were compared, obtaining a maximum relative error of 11%.

On the other hand, the validation of the packed bed was performed based on the experimental work of Hänchen *et al*. [17], where the maximum error in the comparison with the temperature distribution inside the packed bed along the length was 7.2%, while in other evaluated points, the error was less than 3.5%, indicating that the system presents a good performance, see Figure 2.

5. RESULTS AND DISCUSSIONS

The figure 4, presents the daily evolution of the heliostat field efficiency, receiver thermal efficiency, outlet temperature, and thermal power delivered to the receiver for four representative days of the year in Seville, corresponding to spring (day 34), summer (day 124), autumn (day 216), and winter (day 308). In general, all variables increase during the morning, reach their highest values around midday, and then decrease in the afternoon; however, seasonal differences are evident, with summer and autumn showing the highest and most stable thermal performance, while winter exhibits lower values and stronger fluctuations throughout the day. In this case, the date chosen was the 216th.

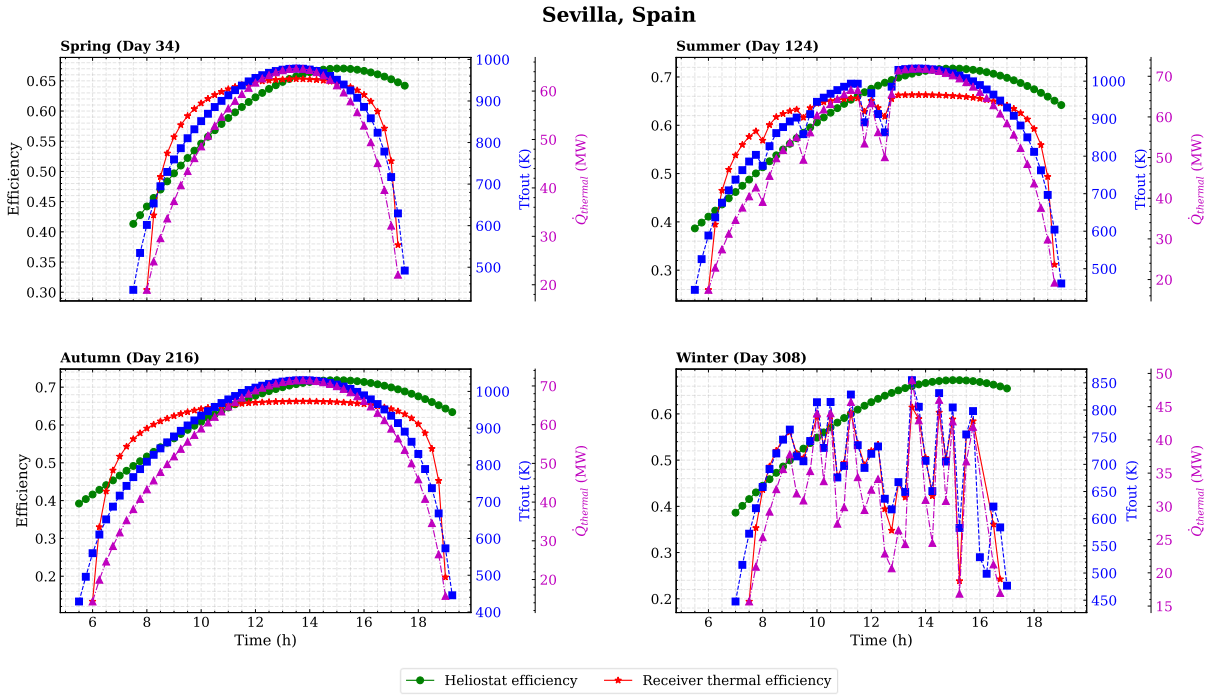

Figure 2. Meteorological data for the city of Seville corresponding to days 34, 124, 216, and 308. The heliostat field efficiency, solar receiver efficiency, receiver outlet temperature, and thermal power supplied to the receiver are shown as a function of time throughout the day.

5.1 System charging processes.

After 4 h of charging, Figure 3 shows a clearly stratified axial temperature distribution along the packed bed. The region close to the hot argon inlet reaches the highest temperatures, on the order of 920–930 K, whereas the opposite end remains at lower temperatures, around 830–860 K. This indicates that, at the end of the charging period, the bed has not been heated uniformly; instead, it exhibits a well-defined thermal front, with a large portion of the bed already heated and an upper section still undergoing thermal transition. Therefore, the dominant temperature gradient is axial, which is consistent with the one-dimensional formulation adopted in this work.

This behavior is consistent with the thermophysical properties of both argon and magnetite. The argon properties, particularly its density, specific heat, viscosity, and thermal conductivity, govern the convective transport of energy and the volumetric heat transfer coefficient, causing the gas to transfer heat more intensely near the inlet while its heating potential decreases as it flows downstream through the bed. In contrast, magnetite provides high thermal inertia due to its high density and temperature-dependent thermophysical properties, allowing the solid matrix to store a significant amount of thermal energy. However, this same thermal storage capacity also delays complete bed homogenization during charging. As a result, after 4 h the system is characterized by a progressive axial thermal front rather than a uniform temperature rise throughout the entire packed bed.

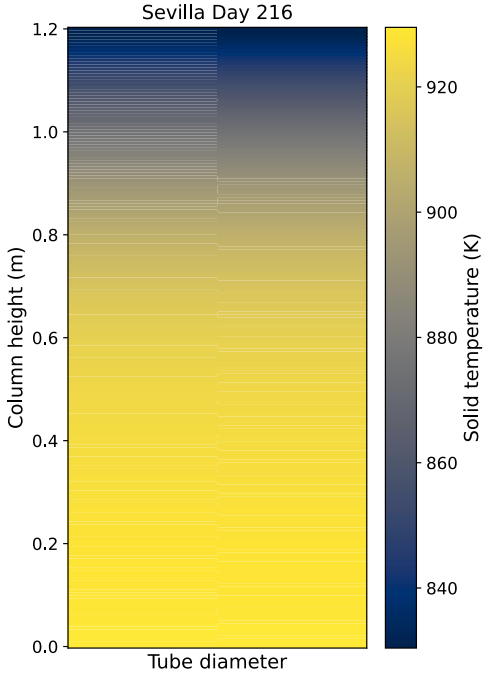

Figure 3. Diagram of the packed bed 4 hours after loading in Seville on the 216th.

5.2 Temperature evolution and power output of the integrated system.

Figure 4 presents the evolution of the charging temperature and the characteristic discharge temperatures at different Brayton-cycle states for the representative days analyzed. During the charging period, the inlet temperature to the packed bed increases rapidly and then remains close to its maximum value, around 920-930 K, although the time required to reach this plateau differs slightly depending on the selected day. During discharge, the temperatures at the different Brayton-cycle stages decrease progressively with time, reflecting the gradual depletion of the thermal energy stored in the packed bed. Among them, the highest temperature corresponds to the turbine inlet condition, while the downstream states exhibit lower values due to the expansion process and subsequent heat recovery. The three representative days show very similar discharge trends, with only small differences in temperature level, indicating that the system response is relatively stable under the selected operating conditions.

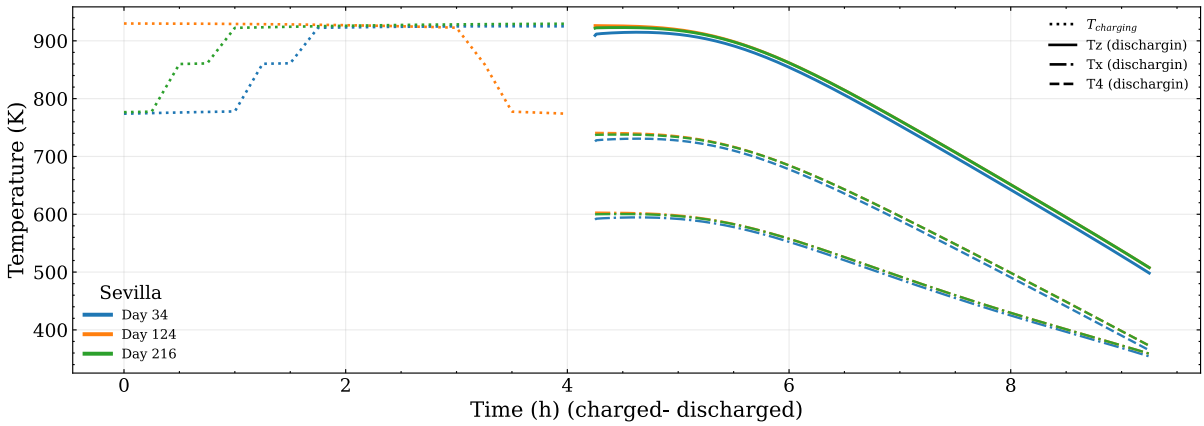

Figure 4: Charge temperature and exhaust temperature in the different stages of the Brayton cycle.

Figure 5 shows the net power produced by the gas turbine Brayton cycle and by the ORC unit during the discharge process. The Brayton-cycle power output decreases continuously with time, from values close to 3 MW at the beginning of discharge to below 1 MW at the end, as a direct consequence of the reduction in the packed-bed outlet temperature and, therefore, of the available turbine enthalpy drop. In contrast, the ORC unit delivers an almost constant power output throughout the discharge period. This behavior is associated with the adjustment of the R600a mass flow rate, which is varied to compensate for the changing heat transferred in the ORC heat exchanger and thus maintain a nearly uniform power production. As a result, the ORC acts as a stabilizing bottoming cycle that recovers residual thermal energy while smoothing the overall power output of the system.

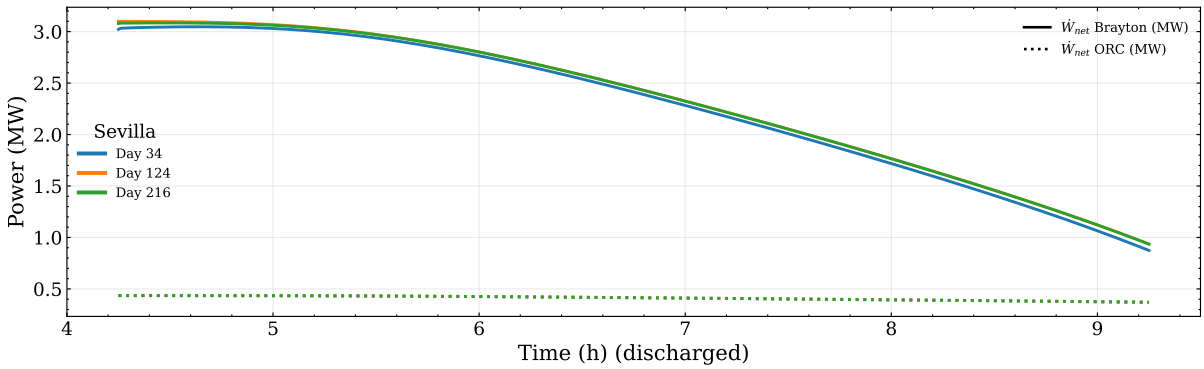

Figure 5: Power generated by the gas turbine and power generated by the ORC turbine.

5.3 Stored energy density and round-trip efficiency.

Figure 6 shows the evolution of the packed-bed stored energy density and the round-trip efficiency (RTE) for the representative days analyzed in Seville. The stored energy density increases continuously with charging time, reaching values slightly above 100 kWh/m³ after 5 h for all cases. This result indicates that the packed bed provides a relatively high volumetric storage capacity, mainly due to the high density of magnetite and its ability to absorb sensible heat over a broad temperature range. The differences among the selected days are small in terms of energy density, which suggests that, once sufficiently high charging temperatures are achieved, the storage medium can accumulate thermal energy in a fairly consistent manner. In contrast, the RTE remains significantly lower, increasing only gradually and reaching values of roughly 20-30%, depending on the day. This reveals that, although the system is effective at storing thermal energy, only a limited fraction of that stored energy is ultimately recovered as net useful work during discharge.

The relatively low RTE can be explained by the cumulative irreversibilities throughout the full charging-discharging chain. First, the useful heat transferred to the working fluid is penalized by the finite effectiveness of the heat exchanger, which is set to 0.70 in the model. Second, the packed bed itself is subject to thermal losses to the surroundings through the wall-loss term included in the energy balance, while the stratified thermal front formed during charging also implies that not all the stored heat is recovered at the highest thermodynamic quality. Third, during discharge, the stored thermal energy must be converted into work through the sCO_2 Brayton cycle and the ORC bottoming cycle, both of which introduce additional exergy destruction and parasitic consumption, particularly due to compression requirements and the progressive

reduction of turbine inlet temperature as discharge proceeds. Therefore, the small RTE should not be interpreted as poor storage capacity of the packed bed itself, but rather as the consequence of converting sensible thermal energy into electricity through a multi-stage system with several sources of irreversibility.

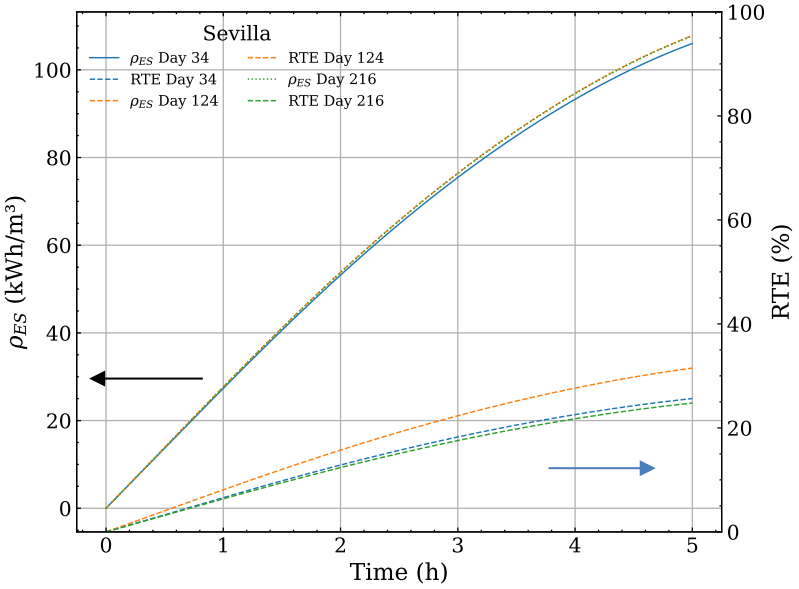

Figure 6: Evolution of packed-bed stored energy density and round-trip efficiency for representative days in Seville.

5.4 Pareto Front Analysis and TOPSIS-Based Solution Selection.

Figure 7 presents the Pareto front obtained by simultaneously maximizing RTE and energy storage density. Because the optimization yields a set of nondominated solutions rather than a unique optimum, TOPSIS was applied to select a compromise solution. A weight of 0.7 was assigned to energy storage density and 0.3 to RTE, prioritizing storage enhancement while still accounting for energy recovery performance. The decreasing shape of the front reflects the expected trade-off between both objectives: increasing the stored energy per unit volume tends to penalize RTE due to the cumulative irreversibilities and thermal losses of the overall charging-discharging process.

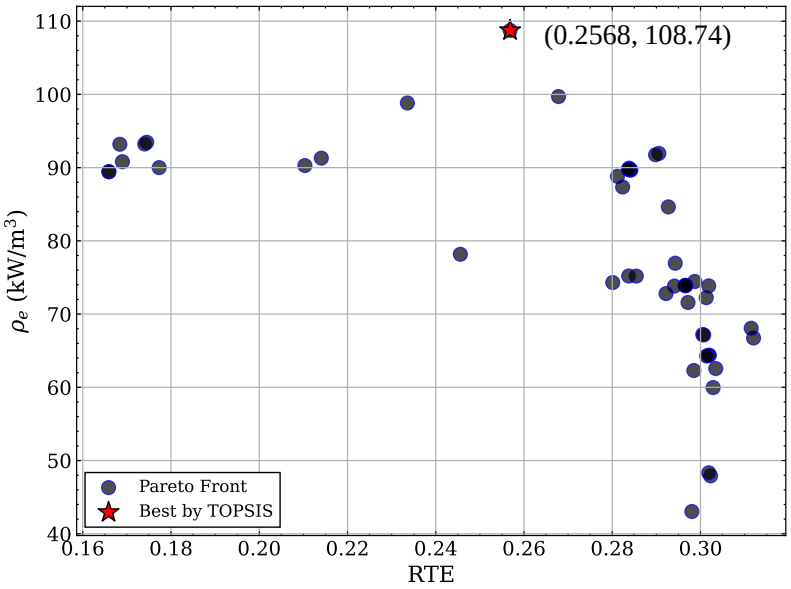

Figure 7: Pareto front obtained for the simultaneous maximization of RTE and energy storage density, with the compromise point selected using the TOPSIS method.

6. CONCLUSIONS

This work demonstrated that the integration of a solar particle receiver with a packed bed thermal energy storage system and an sCO_2 Brayton/ORC discharge block is a technically viable route for improving dispatchability in high-temperature CSP applications. The results showed that the charging process generates a pronounced axial thermal stratification in the packed bed, enabling high storage capacity, while the discharge stage benefits from the Brayton cycle as the main power producer and from the ORC as a stabilizing bottoming cycle for residual heat recovery. At the same time, the study confirmed a clear trade-off between stored energy density and round-trip efficiency, indicating that maximizing storage performance does not necessarily translate into better overall energy recovery. In this sense, the main contribution of the work is not to show a highly efficient system, but to clarify where the thermodynamic penalties arise in the complete charge–discharge chain, particularly in the intermediate heat exchanger, thermal losses in the storage unit, and conversion irreversibilities in the power block. Future work should therefore focus on improving heat exchanger effectiveness, reducing storage losses, extending the analysis to additional climates and operating windows, and incorporating techno-economic and experimental assessments to better establish the real potential of this configuration for next-generation solar tower systems.

Acknowledgments

J.A.Moctezuma-Hernandez acknowledges financial support from CONACYT-México CVU 1006749. The authors acknowledge Universidad de Salamanca and funding from Ministerio de Ciencia, Innovación y Universidades of Spain under grant PID2023-147201OB-I00.

Nomenclature

ρ	Density ($\mathrm{kg/m^3}$)	
T	Temperature	(K)
t	time	(s)
$\mathrm{h_v}$	volumetric heat transfer coefficient ($\mathrm{W/m^3\,K}$)	
V	volume	($\mathrm{m^3}$)

Subscript

s	solid
p	particle
PB	Packed bed
is	isentropic

References

[1] Trevisan, S., Guédez, R., & Laumert, B. (2020). Thermo-economic optimization of an air driven supercritical CO2 Brayton power cycle for concentrating solar power plant with packed bed thermal energy storage. Solar Energy, 211, 1373-1391.

[2] Cu, W., Fang, J., Guo, X., Wei, J., Zheng, N., Chen, K., & Zhou, Z. (2024). Investigation of thermodynamic performances of particle/supercritical CO2 fluidized bed heat exchanger integrated with supercritical CO2 recompression Brayton cycle for concentrated solar power. Energy Conversion and Management, 315, 118805.

[3] Liang, Y., Chen, J., Luo, X., Chen, J., Yang, Z., & Chen, Y. (2020). Simultaneous optimization of combined supercritical CO2 Brayton cycle and organic Rankine cycle integrated with concentrated solar power system. Journal of Cleaner Production, 266, 121927.

[4] Battisti, F. G., de Araujo Passos, L. A., & da Silva, A. K. (2021). Performance mapping of packed-bed thermal energy storage systems for concentrating solar-powered plants using supercritical carbon dioxide. Applied Thermal Engineering, 183, 116032.

[5] Pascual, S., Lisbona, P., & Romeo, L. M. (2022). Thermal energy storage in concentrating solar power plants: a review of European and North American R&D projects. Energies, 15(22), 8570.

[6] Qiu, Y., E, E., & Li, Q. (2023). Triple-objective optimization of SCO2 Brayton cycles for next-generation solar power tower. Energies, 16(14), 5316.

[7] Moctezuma-Hernandez, J. A., Merchán, R. P., & Roco, J. M. M. (2025). Supercritical CO2 hybrid Brayton–Organic Rankine Cycle integrated with a solar central tower particle receiver: Performance, exergy analysis, and choice of the organic refrigerant. Renewable Energy, 250, 123231.
[8] Merchán, R. P., Santos, M. J., Heras, I., Gonzalez-Ayala, J., Medina, A., & Hernández, A. C. (2020). On-design pre-optimization and off-design analysis of hybrid Brayton thermosolar tower power plants for different fluids and plant configurations. Renewable and Sustainable Energy Reviews, 119, 109590.
[9] Copernicus Atmosphere Monitoring Service (ECMWF). (2023). CAMS Radiation Service. https://atmosphere.copernicus.eu/
[10] J. D. McTigue, P. Farres-Antunez, C. N. Markides, A. J. White, et al., “Techno-economic analysis of recuperated Joule-Brayton pumped thermal energy storage,” Energy Conversion and Management, vol. 252, p. 115 016, 2022.386.
[11] K. Okten and B. Kur¸sun, “Thermo-economic assessment of a thermally integrated pumped thermal energy storage (TI-PTES) system combined with an absorption refrigeration cycle driven by low-grade heat source,” Journal of Energy Storage, vol. 51, p. 104 486, 2022.
[12] S. Adewusi and S. M. Zubair, “Second law based thermodynamic analysis of ammonia–water absorption systems,” Energy Conversion and Management, vol. 45, no. 15-16, pp. 2355–2369,391 2004.
[13] A. Sciacovelli et al., “Dynamic simulation of adiabatic compressed air energy storage (A-CAES) plant with integrated thermal storage–link between components performance and plant performance,” Applied Energy, vol. 185, pp. 16–28, 2017. doi: https://doi.org/10.1016/j.apenergy.2016.10.058.
[14] J. P. Coutier and E. Farber, “Two applications of a numerical approach of heat transfer process within rock beds,” Solar Energy, vol. 29, no. 6, pp. 451–462, 1982. doi: https://doi.org/10.1016/0038-092X(82)90053-6.
[13] Y. Ge, Y. Zhao, and C. Zhao, “Transient simulation and thermodynamic analysis of pumped thermal electricity storage based on packed-bed latent heat/cold stores,” Renewable Energy, vol. 174, pp. 939–951, 2021, issn: 0960-1481. doi: https://doi.org/10.1016/j.renene.2021.04.094.
[14] Deb, K., Pratap, A., Agarwal, S., & Meyarivan, T. A. M. T. (2002). A fast and elitist multiobjective genetic algorithm: NSGA-II. IEEE transactions on evolutionary computation, 6(2), 182-197.
[15] Srinivas, N., & Deb, K. (1994). Muiltiobjective optimization using nondominated sorting in genetic algorithms. Evolutionary computation, 2(3), 221-248.
[16] M. A. Reyes-Belmonte, A. Sebastián, J. Spelling, M. Romero, and J. González-Aguilar, “Annual performance of subcritical Rankine cycle coupled to an innovative particle receiver solar power plant,” Renew Energy, vol. 130, pp. 786–795, Jan. 2019, doi: https://doi.org/10.1016/j.renene.2018.06.109.
[17] M. Hänchen, S. Brückner, and A. Steinfeld, “High-temperature thermal storage using a packed bed of rocks–heat transfer analysis and experimental validation,” Applied Thermal Engineering, vol. 31, no. 10, pp. 1798–1806, 2011. doi: https://doi.org/10.1016/j.applthermaleng.2010.10.034.